J. Fluid Mech. (2018), *vol.* 857, *pp.* 851–877. © Cambridge University Press 2018
doi:10.1017/jfm.2018.753

On high-speed impingement of cylindrical droplets upon solid wall considering cavitation effects

Wangxia Wu[1], **Gaoming Xiang**[1] **and Bing Wang**[1,†]

[1]School of Aerospace Engineering, Tsinghua University, Beijing 100084, China

(Received 23 December 2017; revised 16 September 2018; accepted 17 September 2018; first published online 30 October 2018)

The high-speed impingement of droplets on a wall occurs widely in nature and industry. However, there is limited research available on the physical mechanism of the complicated flow phenomena during impact. In this study, a simplified multi-component compressible two-phase fluid model, coupled with the phase-transition procedure, is employed to solve the two-phase hydrodynamics system for high-speed cylindrical droplet impaction on a solid wall. The threshold conditions of the thermodynamic parameters of the fluid are established to numerically model the initiation of phase transition. The inception of cavitation inside the high-speed cylindrical droplets impacting on the solid wall can thus be captured. The morphology and dynamic characteristics of the high-speed droplet impingement process are analysed qualitatively and quantitatively, after the mathematical models and numerical procedures are carefully verified and validated. It was found that a confined curved shock wave is generated when the high-speed cylindrical droplet impacts the wall and this shock wave is reflected by the curved droplet surface. A series of rarefaction waves focus at a position at a distance of one third of the droplet diameter away from the top pole due to the curved surface reflection. This focusing zone is identified as the cavity because the local liquid state satisfies the condition for the inception of cavitation. Moreover, the subsequent evolution of the cavitation zone is demonstrated and the effects of the impact speed, ranging from 50 to 200 m s^{-1}, on the deformation of the cylindrical droplet and the further evolution of the cavitation were studied. The focusing position, where the cavitation core is located, is independent of the initial impaction speed. However, the cavity zone is enlarged and the stronger collapsing wave is induced as the impaction speed increases.

Key words: cavitation, drops, shock waves

1. Introduction

The phenomenon of droplet impaction on solid walls occurs widely in nature and industry such as in raindrops, fuel atomization, ink-jet printing, spray cooling, cutting and cleaning (Yarin 2005; Josserand & Thoroddsen 2016). Understanding the dynamical evolution of droplet impaction has captured the interest of many researchers in the past decades. Up to now, investigations of droplet impaction

†Email address for correspondence: wbing@mail.tsinghua.edu.cn

https://doi.org/10.1017/jfm.2018.753 Published online by Cambridge University Press

problems mainly focused on relatively low speeds, where different droplet sizes, fluid properties and impaction velocities are considered (Mundo, Sommerfeld & Tropea 1995; Pasandideh-Fard *et al.* 1996; Thoroddsen *et al.* 2005; Thoroddsen, Takehara & Etoh 2010, 2012; Eggers *et al.* 2010; Soto *et al.* 2014). However, the erosion or corrosion of pipe walls and steam turbine blades (Ahmad, Casey & Sürken 2009; Xiong, Koshizuka & Sakai 2010, 2011; Okada *et al.* 2011; Xiong *et al.* 2012), is mainly related to high-speed droplet impaction (Sanada, Ando & Colonius 2011; Han, Xie & Zhang 2012; Momber 2016).

To study the flow characteristics in high-speed impingement, theoretical analysis, experimental investigations and numerical simulations were carried out. Cook (1928) derived the theoretical formulation of transient impaction pressure, based on the one-dimensional water hammer theory, which was further improved by Heymann (1969). Due to the high-speed impingement, shockwaves may occur inside the droplet (Bowden & Field 1964). The complex multiple wave structures and an analytical expression of the shock velocity were studied by Haller *et al.* (2003). When the impaction pressure reaches the order of 100 MPa, it is comparable to the material parameters of the defined reference pressure for liquid water and the problem can be regarded as one involving high-speed impingement (Haller *et al.* 2002). Lesser (1981) demonstrated the formation and propagation of the shock wave based on wavelet analysis. The early stage evolution of high-speed droplet impaction was presented by Rein (1993) who also proposed that the focusing of the reflected waves may cause cavitation of the liquid.

Experimental investigations have been conducted to understand the complicated flow characteristics of the high-speed impaction process of the droplet. Hansson & Mørch (1980) tested the effects of cavitation erosion on a metal wall under the collapse of cavity clusters. Furthermore, the impact pressure can be obtained through the examination of the wall damage (Momber 2006; Oka, Mihara & Miyata 2007; Sanada *et al.* 2008; Oka & Miyata 2009; Momber 2016). Sanada *et al.* (2008) proposed that cavitation may occur inside the droplet when it impacts upon a wall with high speed. Using high-speed photography technology, Camus (1971) and Field, Dear & Ogren (1989), Field *et al.* (2012) studied the wave structures inside a cylindrical water column during the impingement, where different column diameters and impaction velocities were examined. Field *et al.* (1989) pointed out that cavitation occurs inside a cylindrical droplet, based on their observations from experimental schlieren images, in which the impaction speed is 110 m s^{-1}. In the case of water cylindrical droplets impacted by a high intensity shock wave, cavitation was observed by Sembian *et al.* (2016) and further numerically verified by Xiang & Wang (2017). However, the above experimental studies have only presented qualitative visualizations of the flow characteristics inside an impacted droplet without any quantitative analysis.

Due to the rapid development of computer technology and the improvement of numerical methods, numerical simulations have become an effective tool to study compressible multiphase flow problems. In 1986, Baer & Nunziato (1986) proposed the seven-equation model for compressible granular flows, known as the Bear–Nunziato model. Saurel & Abgrall (1999) extended the Bear–Nunziato model and developed the Saurel–Abgrall model for compressible gas–liquid two-phase flows. The Saurel–Abgrall model was further developed into different forms, including the full non-equilibrium seven-equation model (Saurel & Abgrall 1999), the reduced six-equation model (Pelanti & Shyue 2014) and the simplified five-equation model (Johnsen & Colonius 2006; Coralic & Colonius 2014). However, these models were not applicable to cavitation inception and cavity collapse, since the effect of phase

https://doi.org/10.1017/jfm.2018.753 Published online by Cambridge University Press

transition is not considered in them. Kondo & Ando (2016) and Niu & Wang (2016) conducted numerical simulations for the problem of high-speed impaction and indicated the existence of cavitation. Unfortunately, the phase transition was not included in their numerical models, and thus, they could not account for a detailed evolution process of cavitation. Therefore, numerical models that consider the effects of phase transition, especially in the cavitation process, are required to study the flow dynamics of high-speed droplet impaction on a solid wall.

An extension of the Saurel–Abgrall model that takes into account the phase transition and contains source terms related to the phase transition has been studied by Saurel, Petitpas & Abgrall (2008), Zein, Hantke & Warnecke (2010), Saurel & Petitpas (2013). Different relaxation approaches were proposed to solve the phase transition source terms (Saurel *et al.* 2008; Han, Hantke & Müller 2017). The basic requirement was to derive an equilibrium state through the relaxation process. Saurel *et al.* (2008) proposed a relaxation approach using Gibbs free energy, in which the equilibrium state was achieved when the Gibbs free energy of the vapour and liquid phase are equivalent. This method was used to simulate problems involving phase transition, such as boiling flows, evaporating liquid jets, cavitating flow in a Venturi nozzle (Saurel, Boivin & Le Métayer 2016) and laser-induced cavitation bubble collapse (Zein, Hantke & Warnecke 2013), but it was not compatible for simulating the bubbly flow, in which the wave dispersion caused by bubble dynamics could not be captured by the barotropic relations (Brennen 2013). For multi-components systems, Han *et al.* (2017) utilized the chemical potential relaxation approach to study the shock bubble interaction problem, in which the effect of partial pressure was considered. The more advanced mixture-averaged models were proposed by Ando, Colonius & Brennen (2011), Fuster & Colonius (2011), which could describe bubbly cavitating flow with bubble dynamics being accounted for. In this study Saurel's model will be employed to capture the phase change in the bulk flow without any existing cavities.

For the transient cavitation process, a specific criterion is essential to trigger the phase transition process in numerical simulations. A liquid can sustain stretched tension before transforming into its vapour phase (Herbert & Caupin 2005). For a certain stretching tension, phase transition will occur if the local pressure exceeds this threshold value, which is called the cavitation pressure (Fisher 1948). Sufficiently pure liquid water is able to withstand pressures lower than -100 MPa (Azouzi *et al.* 2013). Furthermore, the threshold pressure for phase transition varies significantly with the liquid purity (Trevena 1984). The relation between the threshold pressure and temperature, for pure water, was provided by Caupin & Herbert (2006). In this study, we aim to investigate the flow characteristics in high-speed cylindrical droplet impingement on a solid wall through numerical methods.

This paper is organized as follows. In § 2, the physical model of high-speed cylindrical droplet impingement is described, and the governing equations, phase-transition modelling and its numerical treatments are presented. In § 3, the grid sensitivity study is conducted, and the present numerical method is validated. In § 4, the morphology and dynamical evolutions of cylindrical droplet impingement are analysed qualitatively and quantitatively. In § 5, different initial impaction speeds are compared. Finally, the conclusions are presented in § 6.

2. Physical model and numerical procedure

2.1. *Physical model*

In the present numerical study, the high-speed droplet impingement problem will be simulated in two dimensions, as shown in figure 1. There may exist a difference

https://doi.org/10.1017/jfm.2018.753 Published online by Cambridge University Press

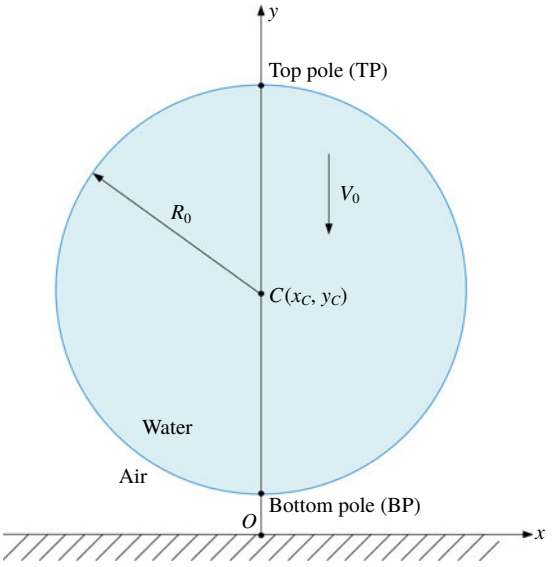


FIGURE 1. (Colour online) Schematic diagram of the high-speed liquid column impingement problem.

between the two-dimensional and three-dimensional simulations. However, it is a challenge to experimentally observe the three-dimensional high-speed droplet during impaction and to obtain the detailed flow field inside the droplet. With the consideration of computational cost, a two-dimensional simulation is carried out in the present study, following the experiment work conducted by Field *et al.* (1989).

The droplet is regarded as a cylindrical liquid column and the water column centre (C), top pole (TP) and bottom pole (BP) are shown in figure 1. The liquid column moves vertically towards the solid wall, at an initial impaction speed of V_0 and initial diameter D_0 (which is equal to $2R_0$) and is taken as 10 mm. The Reynolds number Re, the Weber number We and the Froude number Fr, which characterize the importance of viscous force, capillary force and gravity, respectively, can be computed as follows:

$$Re = \frac{\rho_0 D_0 V_0}{\mu}, \tag{2.1}$$

$$We = \frac{\rho_0 D_0 V_0^2}{\sigma}, \tag{2.2}$$

$$Fr = \frac{V_0^2}{g D_0}, \tag{2.3}$$

where ρ_0, μ, σ and g represent the initial density of the liquid, liquid dynamic viscosity, surface tension coefficient and gravitational acceleration, respectively. Re is 5.8×10^5, We is 3.4×10^5 and Fr is 2.5×10^4, when V_0 is 50 m s^{-1}. Therefore, similar to Kondo & Ando (2016), the effects of viscosity, surface tension and gravity can be neglected in the present study.

2.2. *Governing equations and equations of state (EOSs)*

For highly compressible multi-component two-phase flow that involves phase transition, the governing equations consist of the Euler and scalar transportation

https://doi.org/10.1017/jfm.2018.753 Published online by Cambridge University Press

equations for the volume of fraction. The governing equations are as follows (Saurel *et al.* 2008):

$$\frac{\partial \alpha_k \rho_k}{\partial t} + \nabla \cdot (\alpha_k \rho_k \boldsymbol{u}) = \dot{S}_{\rho,k}, \quad k = 1, \ldots, K, \tag{2.4a}$$

$$\frac{\partial (\rho \boldsymbol{u})}{\partial t} + \nabla \cdot (\rho \boldsymbol{u} \otimes \boldsymbol{u} + p\boldsymbol{I}) = 0, \tag{2.4b}$$

$$\frac{\partial E}{\partial t} + \nabla \cdot [(E + p)\boldsymbol{u}] = 0, \tag{2.4c}$$

$$\frac{\partial \alpha_k}{\partial t} + \boldsymbol{u} \cdot \nabla \alpha_k = \dot{S}_{\alpha,k}, \quad k = 1, \ldots, K-1, \tag{2.4d}$$

where, α_k, ρ_k and $\alpha_k \rho_k$ represent the volume fraction, the density and the value of volume mass of components k, respectively. ρ, $\boldsymbol{u}$, p, $\boldsymbol{I}$, $E = \rho e + (1/2)\rho \boldsymbol{u}^2$ and e are the density, velocity, pressure, unit tensor, total energy and internal specific energy of the mixture, respectively. Three components are included, indicated by the subscripts k can be 1, 2 or 3, which represent the vapour, liquid and air, respectively. The saturation constraint of the volume of fraction yields:

$$\alpha_K = 1 - \sum_{k=1}^{K-1} \alpha_k. \tag{2.5}$$

$\dot{S}_{\rho,k}$ and $\dot{S}_{\alpha,k}$ are the source terms for the volume mass and volume fraction related to the phase transition, which can be respectively expressed as:

$$\dot{S}_{\rho,1} = \dot{m} = \nu(g_2 - \mu_1), \quad \dot{S}_{\rho,2} = -\dot{m} = \nu(\mu_1 - g_2), \quad \dot{S}_{\rho,3} = 0, \tag{2.6a–c}$$

$$\dot{S}_{\alpha,k} = \frac{\dot{m}}{\varrho_k} = \frac{\nu}{\varrho_k}(g_2 - \mu_1), \quad k = 1, 2, \tag{2.7}$$

where $\nu\ (\geqslant 0)$ is the relaxation parameter for the chemical potential, g_2 is the Gibbs free energy of the liquid phase and μ_1 is the chemical potential of the vapour phase, respectively. In the present study, the parameter ν is taken as infinite if the phase-transition condition is satisfied, otherwise it is zero. Therefore, the model is free of parameters. Formulas for the parameters ϱ_k can be found in Zein *et al.* (2010, 2013). For details, please refer to the book of Müller & Müller (2009).

The thermodynamic state of the fluid is described by the stiffened gas equation of state (SG-EOS) (Saurel *et al.* 2008):

$$e_k(p, \rho_k) = \frac{p + \gamma_k p_{\infty,k}}{\rho_k(\gamma_k - 1)} + q_k, \tag{2.8}$$

$$\rho_k(p, T) = \frac{p + p_{\infty,k}}{C_{v,k} T(\gamma_k - 1)}, \tag{2.9}$$

$$h_k(T) = \gamma_k C_{v,k} T + q_k, \tag{2.10}$$

$$g_k(p, T) = (C_{v,k}\gamma_k - q_k')T - C_{v,k} T \log \frac{T^{\gamma_k}}{(p + p_{\infty,k})^{\gamma_k - 1}} + q_k, \tag{2.11}$$

$$\mu_1(T, g_1, \alpha_1, \alpha_2) = g_1 + (\gamma_1 - 1) C_{v,1} T \log \frac{\alpha_1}{1 - \alpha_2}, \tag{2.12}$$

https://doi.org/10.1017/jfm.2018.753 Published online by Cambridge University Press

Components	γ_k	$p_{\infty,k}$ (Pa)	$C_{v,k}$ (J kg^{-1} K^{-1})	q_k (J kg^{-1})	q'_k (J kg^{-1} K^{-1})
Water (vapour)	1.327	0	1200	1.995×10^6	2.410×10^3
Water (liquid)	2.057	1.066×10^9	3449	-1.995×10^6	3.578×10^4
Air	1.4	0	717	0	0

TABLE 1. The parameters involved in the SG-EOS (Han *et al.* 2017).

where, e_k, h_k, g_k and μ_k are respectively internal energy, enthalpy, Gibbs free energy and chemical potential of the considered component; γ_k, $p_{\infty,k}$, $C_{v,k}$, q_k and q'_k are the specific heat ratio, material reference parameter with the dimension of pressure, specific heat capacity at constant volume, heat of formation and entropy constant. The corresponding values of these parameters are listed in table 1. The associated sound speed in each component fluid is given by $c_k = \sqrt{(p_k + p_{\infty,k})\gamma_k/\rho_k}$.

The interface spreads over a few cells due to numerical diffusion in the interface capturing scheme. In this diffuse region, the mixture fluid variables are given as follows (Petitpas *et al.* 2007; Saurel *et al.* 2008; Zein *et al.* 2010):

$$\rho = \sum_{k=1}^{K} \alpha_k \rho_k, \tag{2.13}$$

$$\rho e = \sum_{k=1}^{K} \alpha_k \rho_k e_k, \tag{2.14}$$

$$p = \frac{\rho e - \displaystyle\sum_{k=1}^{K} \alpha_k \rho_k q_k - \sum_{k=1}^{K} \frac{\alpha_k \gamma_k p_{\infty,k}}{\gamma_k - 1}}{\displaystyle\sum_{k=1}^{K} \frac{\alpha_k}{\gamma_k - 1}}, \tag{2.15}$$

$$c = \sqrt{\sum_{k=1}^{K} \frac{\alpha_k \rho_k}{\rho} c_k^2}. \tag{2.16}$$

2.3. *Numerical method*

The finite volume method is used to discretize the governing equations, equation (2.4). A hybrid scheme (Titarev & Toro 2004), which combines the component-wise fifth-order weighted essentially non-oscillatory (WENO) scheme and a second-order monotone upstream centred scheme for conservation laws (MUSCL) scheme, is applied for the spatial reconstructions to the primitive variables. A Godunov-type Harten–Lax–van Leer contact (HLLC) approximate Riemann solver (Toro 2013) is employed to solve the numerical flux at the edges of the cells. In order to adopt the HLLC Riemann solver, referring to the work of Johnsen & Colonius (2006), the advection equation (2.4*d*) is rewritten in a mathematically equivalent form with the chain rule. A third-order total variation diminishing (TVD) Runge–Kutta scheme (Gottlieb & Shu 1998) is utilized for time marching. The source terms, related to the phase transition, are decoupled from the hyperbolic operator, which will be explained in detail in the following section.

https://doi.org/10.1017/jfm.2018.753 Published online by Cambridge University Press

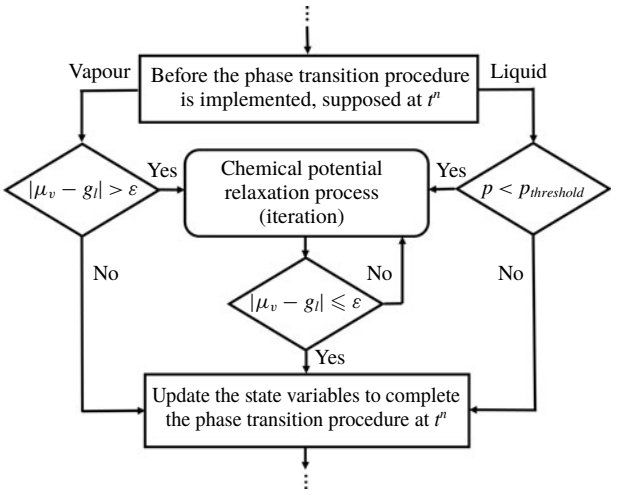


FIGURE 2. The treatment of the phase-transition procedure in the present numerical study.

2.3.1. *Numerical treatment for phase-transition source terms*

For the present compressible two-phase problem, two different phase-transition patterns are involved, the vapour phase transforming into its liquid phase, and the liquid phase transforming into its vapour phase. The physical conditions that trigger the two different phase-transition patterns are introduced separately in this section.

For the vapour phase transforming into its liquid phase, the condition that triggers the phase transition is determined by $p > p_{sat}(T)$, where $p_{sat}(T)$ is the saturated pressure at temperature T. The equivalent condition is that the chemical potential μ_v of the vapour phase is larger than the Gibbs free energy g_l of the liquid phase (Han *et al.* 2017). This is useful for the numerical treatment of the phase-transition source terms. For the liquid phase transforming into its vapour phase, a threshold pressure, $p_{threshold}$, is used to determine when the phase-transition process is triggered. In the present numerical study, with the assumption of pure water, only the homogeneous cavitation process is considered. The value of $p_{threshold}$ is obtained by a linear approximation of the curve of the cavitation pressure of water over the temperature, as per Caupin & Herbert (2006). The mathematical expression is described as follows:

$$p_{threshold} = p_{ref,1} + (p_{ref,0} - p_{ref,1})\frac{(T - T_{ref,1})}{(T_{ref,0} - T_{ref,1})}, \tag{2.17}$$

where, T is the fluid temperature (K), $T_{ref,0}$ and $T_{ref,1}$ are the reference temperatures, taken as 273.15 K and 288.15 K, respectively, and $p_{ref,0}$ and $p_{ref,1}$ are the reference pressures, taken as -115.0 MPa and -100.0 MPa, respectively (Caupin & Herbert 2006). When the local pressure is lower than $p_{threshold}$, the phase transition process is triggered.

Figure 2 shows the flow chart of the numerical treatment of the phase-transition source terms. When the phase-transition condition is satisfied, an instantaneous relaxation process is employed to find the variables in a thermodynamic equilibrium state. Referring to Han *et al.* (2017), relaxation based on the chemical potential is employed for the present numerical study, in which local thermodynamic equilibrium is achieved when $\mu_v = g_l$. According to the conservation of total mass and total

https://doi.org/10.1017/jfm.2018.753 Published online by Cambridge University Press

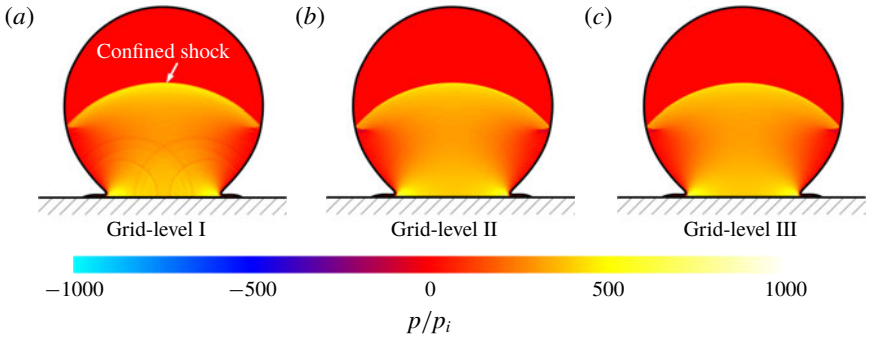


FIGURE 3. (Colour online) Pressure contours under three different grid resolutions, $t = 4.0$ μs.

momentum, the Gibbs free energy of the liquid phase, g_l, and the chemical potential of the vapour phase, μ_v, can both be expressed as a function of phasic density $\alpha_1\rho_1$. The only unknown variable in the equation $\mu_v(\alpha_1\rho_1) = g_l(\alpha_1\rho_1)$ is $\alpha_1\rho_1$ and an iteration procedure is applied to find its value. Then, the other variables can be obtained via their relationship with $\alpha_1\rho_1$. A small value ε, chosen as 10^{-6}, is used to determine whether the iteration convergence is achieved, which is regarded as the thermodynamic equilibrium state from the numerical aspect. Consequently, the other variables at equilibrium state, including p, T and $\alpha_k\rho_k(k \neq 1)$ are obtained. For detailed derivations, readers can refer to Han *et al.* (2017).

2.3.2. *Boundary conditions and initialization*

Figure 1 shows the configuration of the computational domain. The slip wall condition is employed for the bottom boundary of the computational domain, while the Thompson-type non-reflecting boundary condition (Thompson 1987) is employed for the remaining boundaries where only the outgoing waves are evaluated. The liquid and surrounding gas phase are initially in equilibrium with a temperature of 300 K (T_i) and pressure of 1 atm (p_i). The initial velocity of the liquid column is changed for each case; however, the initial condition of the surrounding gas phase remains unchanged for all computation cases. Uniform grids are used for all computations, and the Courant–Friedrich–Lewis (CFL) number is taken as 0.4 for all cases.

3. Numerical verification

3.1. *Grid sensitivity analysis*

The grid sensitivity is analysed by choosing three different grid resolutions: 1.2 (grid-level I), 4.8 (grid-level II) and 10.8 million cells (grid-level III). The grid cells per column diameter correspond to 500, 1000 and 1500, respectively.

The pressure contours for the three different mesh levels at the same instant are shown in figure 3. The extracted pressure profiles along the vertical central axis (y-axis) under three different grid resolutions are shown in figure 4, where pressure is normalized by the initial ambient pressure p_i, and the y coordinate by the initial droplet diameter D_0.

Similar distributions are noticed for the pressure contours of the three different mesh levels, figure 3. It can be found that an obvious pressure jump exists due to the

https://doi.org/10.1017/jfm.2018.753 Published online by Cambridge University Press

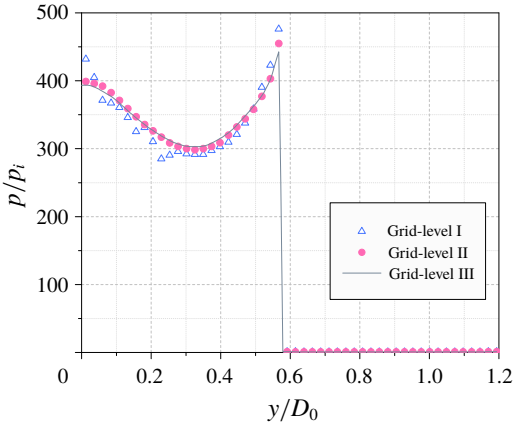


FIGURE 4. (Colour online) Dimensionless pressure along the axial line under three grid resolutions, $t = 4.0$ μs.

confined shock wave (its generation mechanism will be discussed in the following section) for all three grid resolutions at the same position. Slight deviations from the pressure profile are observed behind the shock wave in grid-level I due to the low mesh resolution, while the pressure profiles overlap well for the other two higher grid resolutions. In order to balance the computational efficiency and mesh resolution, the grid level II is finally chosen in the present study.

3.2. *Two-dimensional validation case*

The two-dimensional cylindrical liquid column impaction is simulated. The parameters have the same values as in Field *et al.* (1989). The initial impinging velocity V_0 is 110 m s^{-1}. Figure 5 shows the comparison between the present simulation results and the experimental results from Field *et al.* (1989). For the visualization of the numerical simulations, both the numerical schlieren and pressure contours are shown.

The analysis begins when the column just impacts on the solid wall, figure 5(*a*). Subsequently, the confined shock wave (denoted by S in the experimental image) is generated due to the rapid pressure rising from the impaction region and it propagates downstream away from the initial bottom pole of the column, figure 5(*b*). From then on, the ending points of the confined shock wave propagate along the column surface and the shock wave passes through the water column. The confined shock wave finally touches the top pole of column (TP) until the time shown in figure 5(*g*). Meanwhile, the confined shock wave is reflected by the column surface as it propagates and a series of reflected rarefaction waves are generated. The rarefaction waves interact (denoted by R in the experimental image) and tend to be focused inside the water column due to the curved surface. As the rarefaction waves focus, the pressure of the local fluid becomes very low, figure 5(*j*). Once the local fluid pressure is lower than $p_{threshold}$, a violent phase transition occurs. This phenomenon has been observed both in the experiments and simulations. The last figure obtained by the experiment, figure 5(*j*), shows that a cavitation zone is generated (denoted by the arrow F). For the numerical simulation results, a similar cavitation zone is recognized by the volume fraction of vapour, marked by the solid line shown on the left-hand side of figure 5(*j*). The detailed analysis of the convergence of the reflected rarefaction waves and the generation of cavitation will be presented in the next section.

https://doi.org/10.1017/jfm.2018.753 Published online by Cambridge University Press

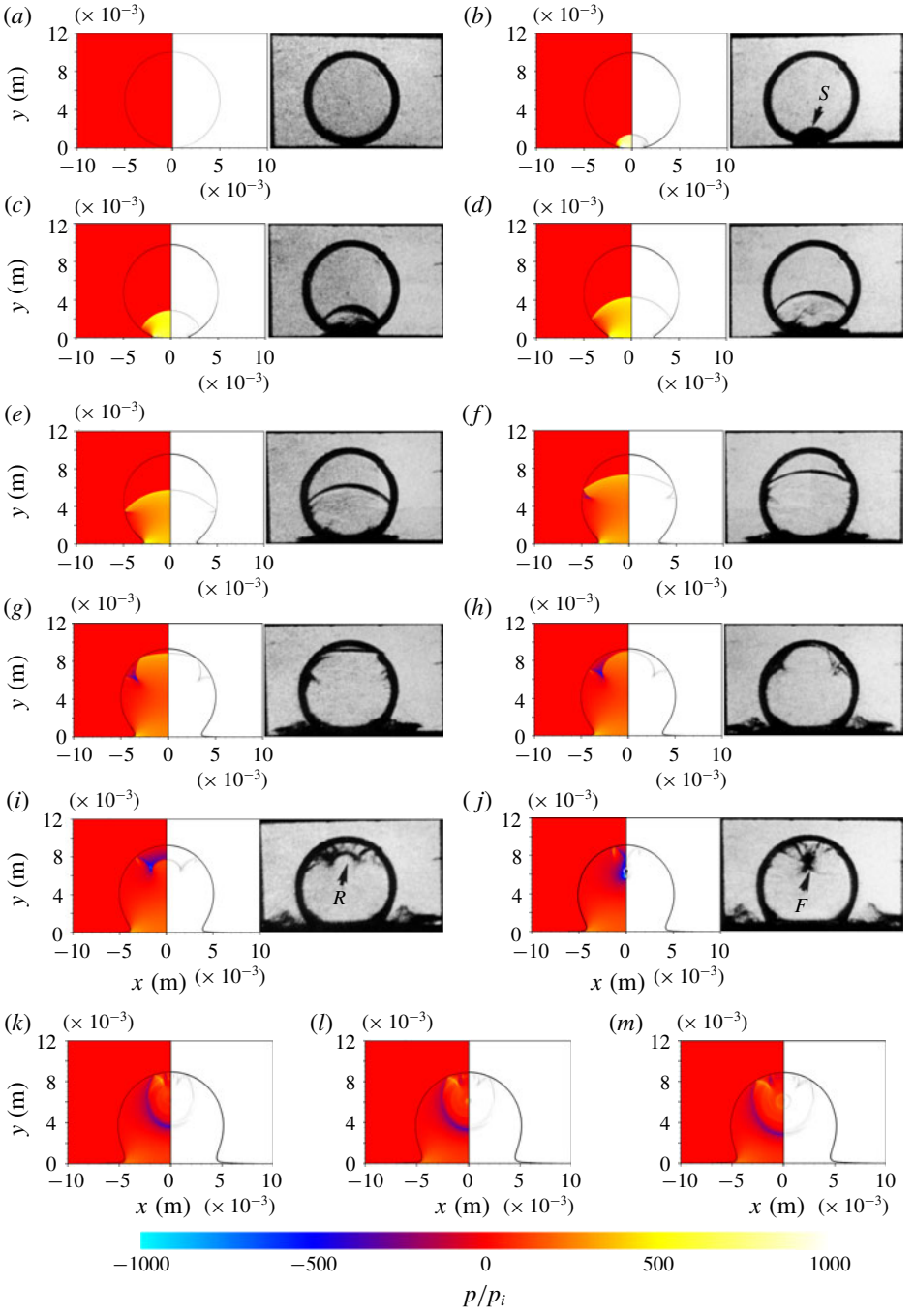


FIGURE 5. (Colour online) Numerical results of the pressure contours (left) and schlieren image (right) of a 10 mm water column impingement with initial speed of 110 m s^{-1} at $t =$ (*a*) 0.0 μs, (*b*) 1.0 μs, (*c*) 2.0 μs, (*d*) 3.0 μs, (*e*) 4.0 μs, (*f*) 5.1 μs, (*g*) 6.2 μs, (*h*) 6.7 μs, (*i*) 7.5 μs, (*j*) 8.7 μs, (*k*) 10.0 μs, (*l*) 10.3 μs, (*m*) 10.6 μs (the cavitation zone extracted from the vapour volume fraction is marked with the solid line). Also shows the experimental schlieren images (*a–j*) with time interval of 1 μs along the impact procedure of Field *et al.* (1989).

https://doi.org/10.1017/jfm.2018.753 Published online by Cambridge University Press

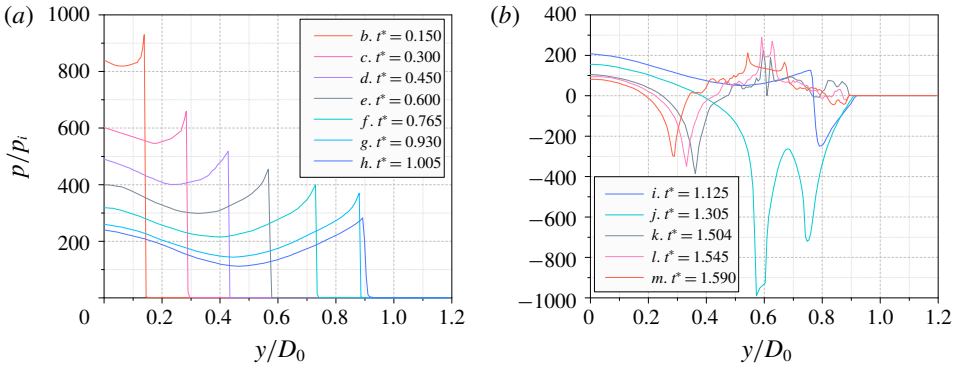


FIGURE 6. (Colour online) The dimensionless pressure profile along the y-axis at different instants of time: (a) related to the time instants of figure 5(b–h), (b) related to the time instants of figure 5(i–m).

Furthermore, the simulation can predict the successive flow process after cavitation occurs. As the droplet continually moves towards the wall, the cavitation collapses as shown from figure 5(k) to figure 5(m). Figure 5(k) corresponds to the time when the cavitation zone has completely collapsed, while figure 5(l) and figure 5(m) show the induced circular shock wave due to the collapse of the cavity. Overall, the simulation results, demonstrating the droplet impinging process, show a good agreement with the experimental flow visualization. The dynamical process of the cavity collapse will be analysed in detail in the next section.

The above comparison shows that the present mathematical models and numerical procedures are able to solve the problem of a cylindrical droplet impinging upon a solid wall. Moreover, the cavitation inception and subsequent collapse that occurs in the impaction process can be well captured by current computation capabilities.

4. Analysis of high-speed impingement of a water column

In this section, a detailed analysis is performed for the water column impingement. The analysis is based on the simulated results obtained when the initial impaction velocity of the cylindrical droplet is 110 m s^{-1}, see § 3.2. In order to understand the physical mechanisms of the flow phenomena, the whole impaction process is divided into two stages, mainly according to the flow characteristics. The propagation and status of the confined shock wave inside the droplet is the main reason for the division of the flow process. In the first stage, the confined shock wave is generated and propagates inside the column (figure 5b–g). The first stage ends when the confined shock wave touches the top pole of the column. The second stage (figure 5h–m) begins and the cavitation inception and collapsing process take place.

The dimensionless time t^* is used, which is the ratio of the physical time over the characteristic time τ ($\tau = D_0/c_0$, D_0 is the initial droplet diameter and c_0 is the sound speed of the droplet liquid under the initial condition), namely, $t^* = t/\tau$. The pressure is non-dimensionalized by the initial ambient pressure p_i. Figure 6 shows the pressure distributions along the vertical central axis inside the water column for the different stages respectively. Figure 6(a) corresponds to the time instants of figure 5(b–h) in the first stage. Figure 6(b) corresponds to the following series in the second stage.

https://doi.org/10.1017/jfm.2018.753 Published online by Cambridge University Press

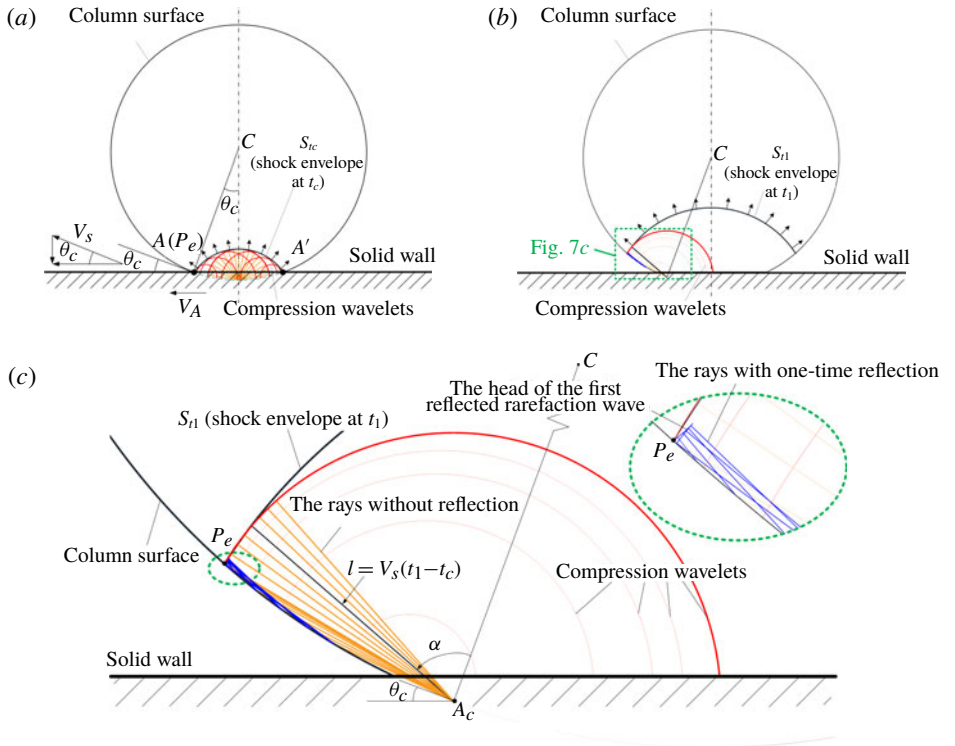


FIGURE 7. (Colour online) Schematic diagram of the generation of confined shock and the ray analysis: (*a*) the schematic diagram at critical time t_c; (*b*) the schematic diagram at the time instant, t_1, which is selected at the instant after the critical time; (*c*) the enlarged view of the schematic diagram at t_1 ($\overline{CA_c}$ is the line between the critical contact point A_c and the water column centre C).

4.1. *The first stage*

The first stage begins at t_0 when the water column just impacts the solid wall. There is a contact line segment $\overline{AA'}$ between the water column and the solid wall and A coincides with A' at t_0. Furthermore, we only considered the left contact point A for the following analysis because flow is symmetric. It is obvious that A is moving with velocity V_A along the x-axis during the impaction of the column. The contact angle θ is defined as the angle between the solid wall and the tangent line of the liquid column at A. The value of θ is zero when the water column just impacts the solid wall, and V_A is much higher than the local liquid sound speed at this time. By the Huygens principle (Haller *et al.* 2003), at each time instant, an individual compression wavelet will be emitted at A that will propagate with the local sound speed. Accounting for the acoustic limit (Lesser 1981) of the compression wavelet, V_A is higher than the propagation speed of the wavelet at the early stage of the impaction, which means that the emitted compression wavelets cannot exceed the contact point A.

These compression wavelets form a shock envelope, denoted as S_t, figure 7(*a*). As the shock wave is constrained inside the column, this shock envelope S_t is also called a confined shock (Obreschkow *et al.* 2011). Initially, the ending point of the confined shock (denoted as P_e) remains attached to the solid wall and overlaps with A. Since V_A decreases gradually, the x-component velocity of P_e will catch up with V_A and the

https://doi.org/10.1017/jfm.2018.753 Published online by Cambridge University Press

confined shock will detach itself from the solid wall. We define the time when the confined shock just detaches itself from the solid wall as the critical time t_c. If $t < t_c$, the end points of the shock envelope are attached to the solid wall and P_e overlaps with A. If $t > t_c$, the shock envelope will detach itself from the solid wall and P_e will propagate along the column surface above the solid wall. At the critical time t_c, the critical contact angle θ_c at the critical contact point A_c is derived from the following expression (Rein 1993):

$$\tan\theta_c = \frac{V_0}{V_{A,c}} = \frac{V_0}{\sqrt{V_s{}^2 - V_0^2}}, \tag{4.1}$$

where $V_{A,c}$ is the velocity of A_c and V_s is the velocity of P_e, obtained from Heymann (1969), which yields:

$$V_s = c_0 + \chi V_0, \tag{4.2}$$

where c_0 is the sound speed of the liquid in the unshocked region and χ is a constant that depends on the liquid property. For water, χ is taken as 2.0 according to Heymann (1969) and 1.921 according to Haller *et al.* (2002). Both values of χ are very close to each other in these two references, however, in this study we assume the value suggested by Heymann (1969). Subsequently, the critical angle θ_c calculated from (4.1) is 3.6° ($V_0 = 110$ m s^{-1}). Referring to Heymann (1969), the water hammer pressure, the maximum pressure at the initial impact point (O), is defined as:

$$p_h = \rho_0 V_0 V_s, \tag{4.3}$$

where V_s is the velocity of the initial confined shock wave, calculated by (4.2).

It is inferred from figure 6(*a*) that the confined shock propagates upward, and its strength gradually decreases as it detaches from the solid wall. The confined shock can be equivalent to an explosion wave with a certain arc length whose strength gradually decreases as it propagates outwards.

As the ending points of the confined shock wave detach from the solid wall, the shock wave propagates inside the water column and moves towards the top pole, as shown in figure 7(*b*). The reflected and transmitted waves are generated on the curved column surface. Since the acoustic impedance $\rho_l c_l$ in water is much larger than that in air, the reflected waves should be rarefaction waves and the transmitted waves should be shock waves. The transmitted shock wave is so weak that it is almost invisible in the numerical schlieren images.

The path of the rays tracing the compression wavelets is demonstrated to understand the evolution of different types of waves. In figure 7(*a*), a series of rays pointed in different specified directions is used to demonstrate the evolution of each compression wavelet emitted from the contact point. From one contact point, the rays represent the paths of the compression wavelet and the length of the rays is equal to the propagation distance of the compression wavelet. Meanwhile, the rays will be reflected symmetrically on the curved column surface. In this stage, the situation at the critical time t_c is chosen to analyse the rays emitted from the contact point A_c, figure 7(*a*), which emits the last compression wavelet that can catch up with the confined shock. This wavelet propagates upwards for a certain time, for example at time instant t_1, and the wave structures and the emitted rays are shown in figure 7(*b*).

In figure 7(*c*), which is the intersection angle, the emitting angle of each ray is the angle between any arbitrarily chosen ray and the line segment $\overline{CA_c}$. We can use the dimension of such an angle to analyse the reflection behaviour of the traced wavelet.

https://doi.org/10.1017/jfm.2018.753 Published online by Cambridge University Press

The emitting angle α lies in $[0, \pi/2]$. At a specific instant, t_1, the range of the ray l is computed by $l = c(t_1 - t_c)$, where c is the local sound speed. If the compression wavelet is reflected from the column surface, l will represent the total range of the ray before and after reflection. The compression wavelet will be reflected more than once from the column surface. The reflection times are related to the angular dimension of α and the present time, which are elaborated as follows:

If the emitted rays are not reflected at an instant t, the emitting angle α will satisfy:

$$\alpha \leqslant \arccos \frac{l}{2R} = \arccos \frac{c(t - t_c)}{2R}. \tag{4.4}$$

If the rays are reflected N times ($N = 1, 2, 3, \ldots$), angle α will satisfy:

$$\arccos \frac{c(t - t_c)}{2RN} = \arccos \frac{l/N}{2R} < \alpha \leqslant \arccos \frac{l/(N+1)}{2R} = \arccos \frac{c(t - t_c)}{2R(N+1)}. \tag{4.5}$$

Thus, different intervals of the angle α, according to the reflection times of a ray, exist.

The shock envelope is formed by the infinite emitted compression wavelets before the critical time t_c. The compression wavelet emitted from the critical contact point A_c is part of the confined shock envelope and it is the nearest wavelet to the column surface. The reflection of this compression wavelet also represents the reflection of the confined shock on the column surface. The discussion about the evolution of this compression wavelet is helpful to understand the character of the confined shock wave close to the column surface. The rays that belong to this compression wavelet start to be reflected on the column surface once they are emitted from the critical contact point A_c. For $\alpha \in (\arccos(c(t_1 - t_c)/2R), \arccos(c(t_1 - t_c)/4R)]$, the rays will be reflected once, and their ending points represent the head of the first reflection waves (the rarefaction waves), figure 7(*c*). Similarly, for $\alpha \in (\arccos(c(t_1 - t_c)/4R), \arccos(c(t_1 - t_c)/6R)]$, the rays will be reflected twice, and their ending points represent the head of the second reflection waves (the compression waves). Thus, the position of the head of the Nth reflection waves are known.

Meanwhile, as the water column continues to impact on the solid wall later than the critical time t_c, compression wavelets are continuously generated, however, they never catch up with the confined shock envelope, figure 7(*c*). The behaviour of these compression wavelets is similar and their strength becomes very weak. Nonetheless, we will not elaborate further on this in the present study.

As the confined shock wave propagates upwards, the reflected rarefaction waves are observed behind the confined shock and a certain time, $t^* = 0.81(t_2)$, is chosen for the following analysis. The numerical schlieren, the pressure contour together with the schematic of the emitted rays belonging to the compression wavelet, are shown in figure 8. The position and shape of the reflected rarefaction waves are obtained from the analysis of the emitted rays.

Figure 8(*b*) shows the emitted rays that belong to the non-reflected confined shock, the first reflected rarefaction, and the second reflected compression wave. Five regimes of the emitted rays exist, figure 8(*b*), which are divided based on the value range of the emitting angle α, including (I), $0 < \alpha \leqslant \alpha_0$; (II), $\alpha_0 < \alpha \leqslant \alpha_1$; (III), $\alpha_1 < \alpha \leqslant \alpha_2$; (IV), $\alpha_2 < \alpha \leqslant \alpha_3$; and (V), $\alpha_3 < \alpha \leqslant \alpha_4$. In regimes (II) and (III) the emitted rays are reflected once and in regimes (IV) and (V) the emitted rays are reflected twice. As shown in figure 8(*c*), in regime (I), $\alpha_0 = \arccos(c(t_2 - t_c)/2R)$ according to (4.4), the propagating head of these continuously emitted rays forms

https://doi.org/10.1017/jfm.2018.753 Published online by Cambridge University Press

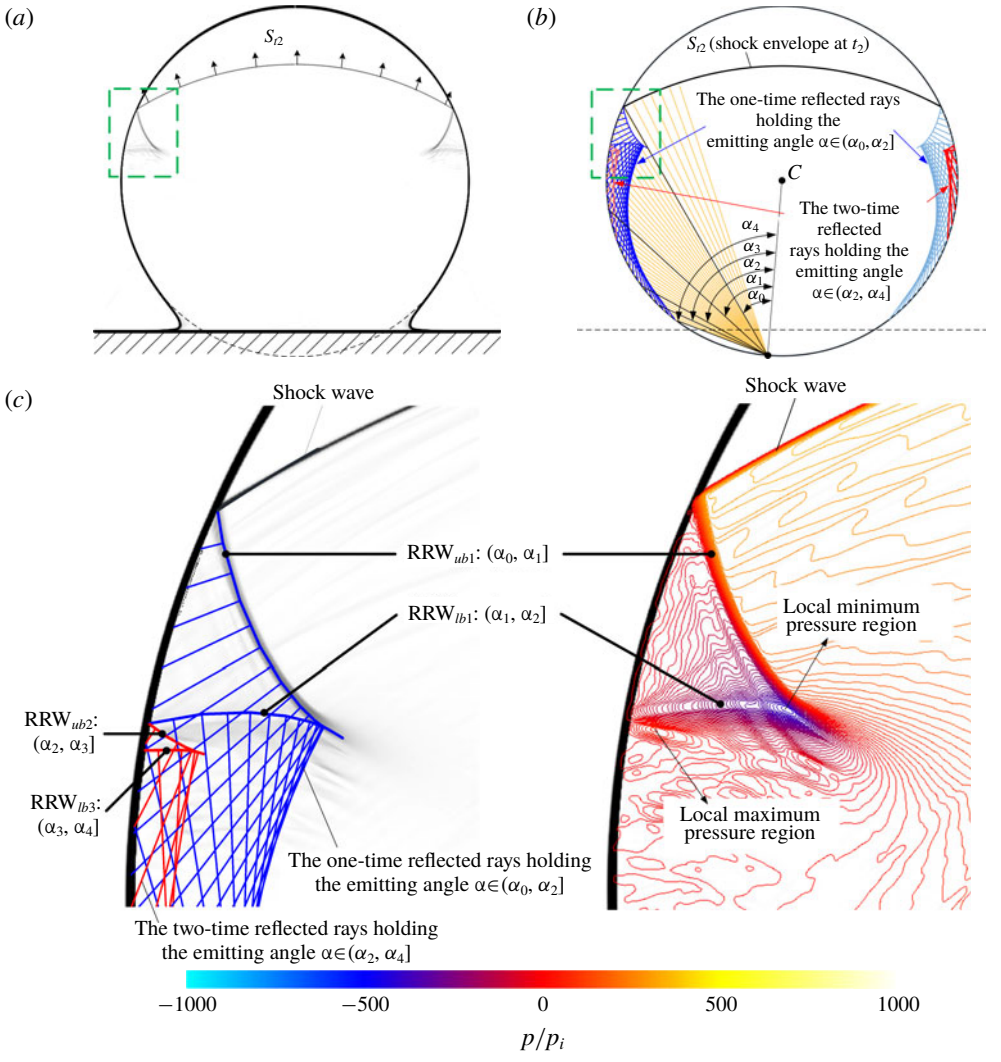


FIGURE 8. (Colour online) Computational results and the schematic diagram of ray analysis in the first stage at the time instant, $t^* = 0.81(t_2)$: (*a*) the numerical schlieren contour; (*b*) the schematic diagram of ray analysis; (*c*) the partial enlarged view of the area of the dashed rectangle in figure 8(*a*,*b*). The left side presents the comparison between schematic diagram and numerical schlieren contour, while the right side presents the corresponding numerical result of pressure isolines.

the confined shock envelope (S_t). In regime (II), the value of α_1 lies between α_0 and α_2 and the propagating head of the continuously emitted rays forms the upper branch of the head of the first reflected rarefaction waves (RRW_{ub1}). In regime (III), $\alpha_2 = \arccos(c(t_2 - t_c)/4R)$ according to (4.5), the propagating head of the continuously emitted rays forms the lower branch of the head of the first reflected rarefaction waves (RRW_{lb1}). In regime (IV), the value of α_3 lies between α_2 and α_4 and the propagating head of these continuous emitted rays forms the upper branch of the second reflected compression waves (RCW_{ub2}). In regime (V), $\alpha_4 = \arccos(c(t_2 - t_c)/6R)$ according to

https://doi.org/10.1017/jfm.2018.753 Published online by Cambridge University Press

(4.5), the propagating head of the continuously emitted rays forms the lower branch of the second reflected compression waves (RCW_{lb2}).

The analytical shape and position of the first reflected rarefaction waves (RRW_{ub1} and RRW_{lb1}) overlap well with those visualized by the numerical schlieren results, figure 8(*c*). The second reflected compression waves are too weak to be observed from the numerical schlieren results. From the pressure isolines, figure 8(*c*), the marked local maximum pressure region validates the second reflected compression waves and its location is also consistent with the analytical results. Ideally, the emitted rays can be reflected infinite number of times, while the other generated reflected waves are much weaker except for the first and second reflected waves. Therefore, they cannot be recognized in the numerical schlieren contour or in the pressure isolines.

In addition, due to the superposition of the first reflected rarefaction waves, and also indicated by the emitted rays, a local minimum-pressure region is observed, figure 8(*c*). Meanwhile, the pressure behind the lower branch of the first reflected rarefaction waves is recovered, because the subsequent emitting compression wavelets catch up with these rarefaction waves.

4.2. *The second stage*

The second stage begins when the confined shock S_t reaches the TP of the water column at the time instant $t^* = 0.975(t_3)$. The analytical schematic is presented in figure 9, which demonstrates the first reflected rarefaction wave evolution. The numerical schlieren contours at $t^* = 0.975(t_3)$ and $t^* = 1.305(t_4)$ are shown in figures 9(*b*) and 9(*d*), respectively.

When all the rays initially emitted from BP are drawn, which are reflected once, the envelope of these first reflected rays is obtained, figure 9(*a*). The intersection points of RRW_{ub1} and RRW_{lb1} always lie on this envelope upon propagation of the reflected rarefaction wave. From the schematic of RRW_{ub1} and RRW_{lb1} at four different time instants, which can be derived from similar analysis in § 4.1, it is observed that the intersection points of RRW_{ub1} and RRW_{lb1} move along the envelope from time t_2 to t_3. When the uppermost point of the confined shock arrives at TP of the water column, the confined shock is totally reflected. The two branches of RRW_{ub1}, from the left and right sides, meet at the vertical central axis and an arched RRW_{ub1} is formed with the two RRW_{lb1} following on the left and right sides. The propagating directions of the combined arched RRW_{ub1} and the two separated RRW_{lb1} from the left and right sides are shown in figure 9(*b*). This indicates that the combined arched RRW_{ub1} focuses inside the water column.

Five different time instants from time t_3 to t_4 are chosen to schematically demonstrate the evolution process of RRW_{ub1} and RRW_{lb1}, figure 9(*c*). The curvature radius of the arched RRW_{ub1} gradually decreases as the reflected rarefaction waves propagate. Finally, the combined arched RRW_{ub1} focuses on the vertical central axis and the focusing point is named P_f, figure 9(*c*). Meanwhile, the two following RRW_{lb1} become wider as they propagate upstream. The intersection point of RRW_{ub1} and RRW_{lb1} keeps moving along the envelope of the reflected rays with one-time reflection.

As the one-time reflected rays are related to the propagation of the first reflected rarefaction wave, we can use these one-time reflected rays to analyse the position of P_f of the arched RRW_{ub1}. As shown in figure 9(*c*), the envelope of the one-time reflected rays corresponds to their limiting boundary and the reflected rays are concentrated on their envelope. The concentrated reflected rays represent

https://doi.org/10.1017/jfm.2018.753 Published online by Cambridge University Press

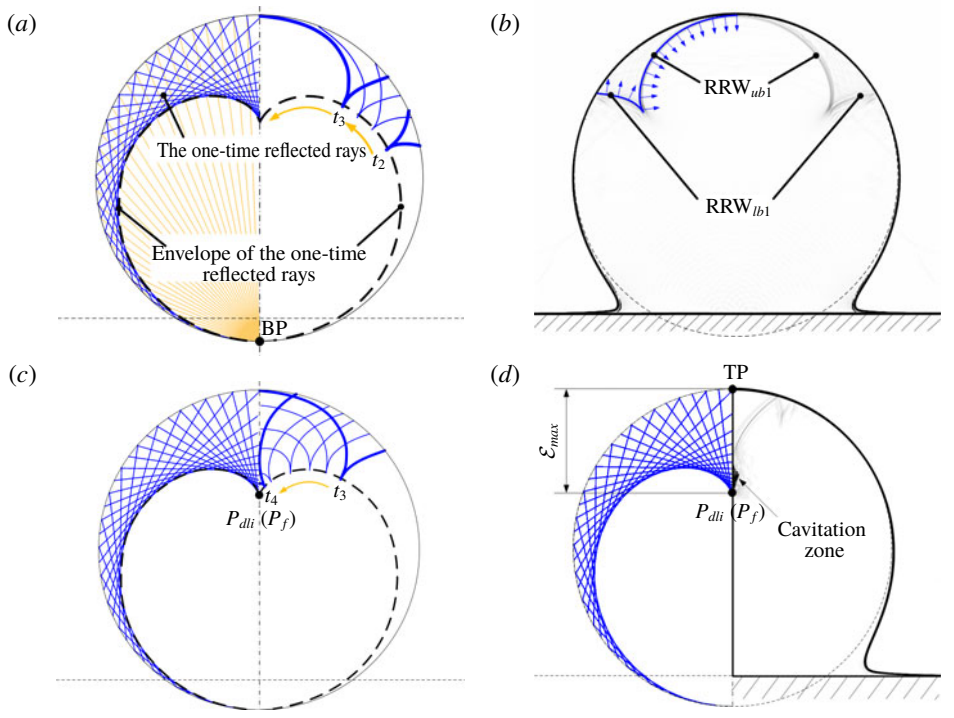


FIGURE 9. (Colour online) (*a*) All the first reflected rays emitted from BP with the original angle of the interval [0, $\pi/2$] (*a*,*c*), the schematic diagram of the first reflected rarefaction wave propagation from $t_2(t^* = 0.81)$ to $t_3(t^* = 0.975)$ (*b*,*d*). (*b*) The numerical schlieren contour at $t^* = 0.975(t_3)$. (*c*) The schematic diagram of the first reflected rarefaction wave propagation from $t_3(t^* = 0.975)$ to $t_4(t^* = 1.305)$. (*d*) The numerical schlieren contour at $t^* = 1.305(t_4)$.

the superposition of the RRW_{ub1} and RRW_{lb1}, which is related to the local minimum-pressure region at each time instant, figure 8. The envelopes of the left and right sides interact on the vertical central axis. The intersection point is also the downward limiting position of the one-time reflected rays that intersect with the vertical central axis, and is named the downward limiting intersection point, P_{dli}, figure 9(*d*).

The position of P_{dli} can be obtained theoretically according to the ray analysis (Obreschkow *et al.* 2011). Figure 10 shows a series of rays emitted from the BP with the emitting angles α holding the interval of [0, $\pi/4$], where the one-time reflected rays can intersect with the vertical central axis. If an arbitrary ray (the black solid lines with an arrow) is chosen, the distance δ between the intersection point P_i (the intersection point of the first reflected ray with the vertical central axis) and the TP of the column can be expressed as follows:

$$\delta = R_0 - \frac{\sin\alpha \cdot R_0}{\sin\gamma}, \tag{4.6}$$

https://doi.org/10.1017/jfm.2018.753 Published online by Cambridge University Press

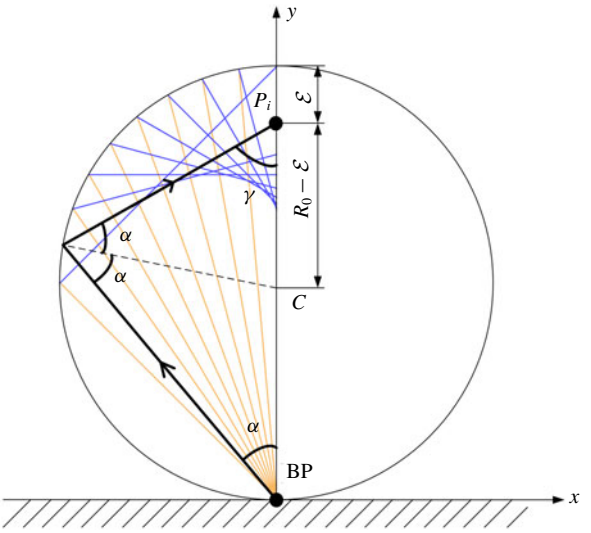


FIGURE 10. (Colour online) Schematic diagram for the intersection point between the reflected rays, with one-time reflection, and the vertical central axis.

where R_0 is the initial radius of the water column. The intersection angles α and γ are shown in figure 10. The distance δ can be rewritten as follows:

$$\delta = R_0 - \frac{R_0}{3 - 4\sin^2\alpha}, \tag{4.7}$$

where $\alpha \in [0, \pi/4]$. A maximum limiting value of δ exists, thus, the position of P_{dli} of the one-time reflected rays is obtained, which has the following expression:

$$\delta_{max} = \lim_{\alpha \to 0} \left(R_0 - \frac{R_0}{3 - 4\sin^2\alpha} \right) = \frac{2}{3} R_0 = \frac{D_0}{3}, \tag{4.8}$$

where D_0 is the initial diameter of the water column.

The above expression for determining the position of P_{dli} corresponds to the rays initially emitted from one contact point (i.e. from one wavelet). We observed that P_{dli} overlaps with P_f, which indicates that RRW_{ub1} finally focuses at a position 1/3 of the droplet diameter away from TP, figure 9(*c*). In fact, there are an infinite number of emitted wavelets forming the shock envelope before the critical time t_c. They also focus on the same limiting intersection point (P_{dli}) at the same time instant, based on a similar analysis of the emitted ray, however, they are not shown here. In another aspect, the arched RRW_{ub1} that corresponds to the infinite reflected rays at each time instant, the focusing point of these infinite rays and the P_f that corresponds to RRW_{ub1}, are consistent.

Due to the focusing effect of the reflected rarefaction waves, a local low-pressure zone is created in the stretched liquid. Therefore, the pressure around P_f is significantly lowered and reaches a value below the $p_{threshold}$, which means that the transient phase-transition process is triggered, and cavitation occurs. Subsequently, the cavity will grow to be a visible cavitation zone. The predicted position of P_f fits well with that of the observations, both in the experimental and numerical results, figures 5(*j*) and 9(*d*).

https://doi.org/10.1017/jfm.2018.753 Published online by Cambridge University Press

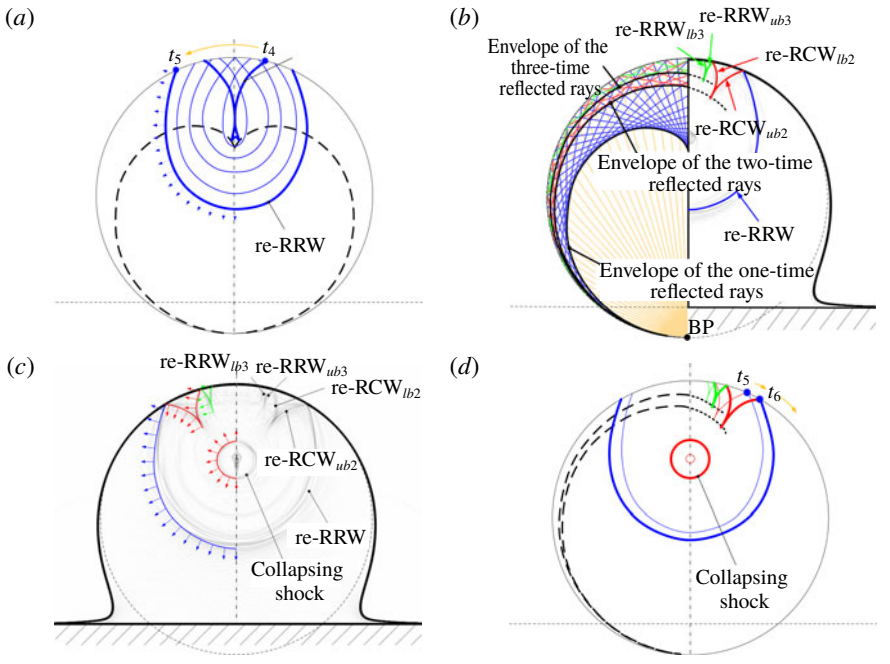


FIGURE 11. (Colour online) (*a*) Schematic diagram of the first reflected rarefaction wave propagation from t_4 ($t^* = 1.305$) to t_5 ($t^* = 1.545$). (*b*) All of the emitted rays from BP with one-, two- and three-time reflection with the original angle of the interval $[0, \pi/2]$ (*a*,*c*), and the numerical schlieren contour at time t_5 ($t^* = 1.545$) (*b*,*d*). (*c*) Numerical schlieren contour at time t_6 ($t^* = 1.59$). (*d*) Schematic diagram of the reflected waves' propagation from t_5 ($t^* = 1.545$) to t_6 ($t^* = 1.59$).

So far, we have analysed the spatio-temporal evolution of the confined shock and the first reflected rarefaction wave before RRW$_{ub1}$ focuses on the vertical central axis. Subsequently, the complicated multi-reflected waves and the cavity collapse inside the droplet will appear. We will try to elaborate on these further in this section.

Six typical time instants from t_4 to t_5 are chosen to demonstrate the evolution of the RRW$_{lb1}$, figure 11(*a*). The two branches of symmetrical RRW$_{lb1}$, from the left and right sides, will interact with each other and be reflected at the vertical central axis. After the interaction among the left reflected RRW$_{lb1}$, the right reflected RRW$_{lb1}$ and the re-expanding wave from the focusing point, an expanding re-reflected rarefaction wave (re-RRW) is formed. The shape and position of the re-RRW at $t^* = 1.545$ (t_5) are shown in the numerical schlieren contour, figure 11(*b*). Two other waves are also observed, which are the second reflected compression wave and the third reflected rarefaction wave, respectively. The peak-pressure value induced by the second reflected waves (compression waves) is 6.31×10^7 Pa, which is approximately 33 % of p_h. The peak-pressure value induced by the third reflected waves (rarefaction waves) is -3.0×10^7 Pa, whose absolute value is approximately 16 % of the value of p_h. Therefore, the strength of the reflected waves decreases gradually due to multiple reflections. As shown in figure 11, the repeated reflection waves cannot be clearly observed since they are much weaker. The RCW$_{ub2}$, RCW$_{lb2}$, RRW$_{ub3}$ and RRW$_{lb3}$ propagating from the left and right sides interact with each other and reflect on the vertical central axis. These reflected waves are denoted as re-RCW$_{ub2}$, re-RCW$_{lb2}$,

https://doi.org/10.1017/jfm.2018.753 Published online by Cambridge University Press

Initial speed V_0 (m s^{-1})	50	110	150	200
Analytical θ_c (deg.)	1.8	3.6	4.8	6.0
Numerical θ_c (deg.)	1.8	3.7	4.9	6.1

TABLE 2. The analytical and numerical θ_c for different initial impaction speeds.

re-RRW$_{ub3}$ and re-RRW$_{lb3}$, respectively. The reflected wave structures are clearly presented in the numerical schlieren contour, figure 11. The upper concave re-RRW expands towards the bottom wall and is followed by the second and third reflected waves at the end. The intersection points of the upper and lower branches of the second and third reflected waves are moving along the envelopes extracted from the ray analysis, figure 11(*d*). Three curves related to the envelopes are presented, including the lower, middle and upper branches, figure 11(*b*). They represent the trajectories of the intersection points of the upper and lower branches of the first, second and third reflected waves, respectively.

As the re-RRW propagates outward, the cavity caused by the focusing of RRW$_{ub1}$ collapses. The peak pressure during the collapsing of the cavity reaches 81 MPa, which is about 800 times the initial ambient pressure for the present case (initial impaction speed $V_0 = 110$ m s^{-1}). From the numerical schlieren contours shown in figure 11(*b*,*c*), a circular shock wave, which is known as the collapsing shock, is found as the cavity collapses and explodes outwards. Finally, the collapsing shock will reach the bottom wall, the results at this time are not shown, and potentially damage it.

To summarize, combining numerical simulation with theoretical approximation, the unsteady wave structures (including the confined shock, the multi-reflected waves and the cavitation collapsing shock), inside the droplet during the impingement of a high-speed cylindrical droplet on a solid wall are carefully analysed. The properties of the waves and their evolution processes inside the droplet are elucidated with the help of the ray analysis, which, to the authors' knowledge, are not clarified in the previously available literatures.

5. Effects of impaction speed

In this section, different initial impaction speeds, 50, 110, 150 and 200 m s^{-1}, are considered for the water column impaction on a solid wall.

Both the analytical (calculated by (4.1)) and numerical values of the critical angle, θ_c, under the different impaction speeds are shown in table 2; θ_c increases with the increase of the initial impaction speed. The temporal variations of the characteristic scales, including the length d_l and width d_w, of the water column, figure 12, are normalized by the initial column diameter; d_l is defined as the distance from the wall to TP and d_w is defined as the diameter along the centre of the column in the horizontal direction. It is observed that d_l of the column decreases, while d_w increases, with time as the water column impacts on the wall. The decreasing rate of d_l is larger for higher initial impaction speed. At $t^* = 1$ the curve has a turning point for each chosen impaction speed, figure 12(*a*). This is the exact time when the confined shock arrives at the TP of the column. The width of the column keeps unchanged until $t^* = 0.6$, then it increases rapidly for all the chosen impaction speeds, as shown in figure 12(*b*).

https://doi.org/10.1017/jfm.2018.753 Published online by Cambridge University Press

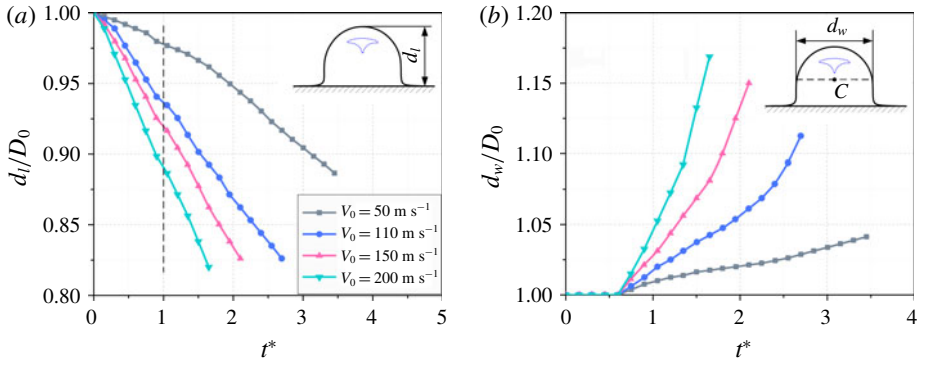


FIGURE 12. (Colour online) The time evolution of the dimensionless length (*a*) and width (*b*) of the water column.

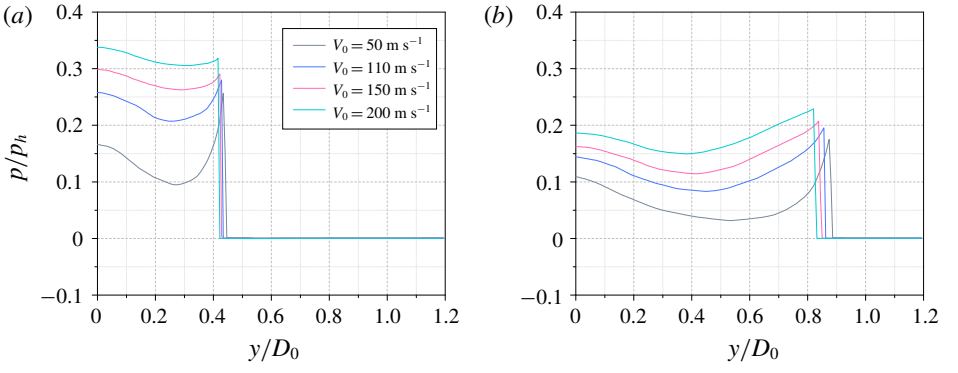


FIGURE 13. (Colour online) Dimensionless pressure value along the vertical central line for the four simulation cases at time instants $t^* = 0.45$ (*a*) and $t^* = 0.9$ (*b*).

The pressure distributions along the vertical central line for the different cases that non-dimensionalized by each corresponding water hammer pressure p_h (calculated by (4.3)) at the dimensionless times of $t^* = 0.45$ and $t^* = 0.9$ are shown in figure 13. It is found that the confined shock wave will be strengthened with a higher initial impaction speed, as the pressure behind the confined shock wave is much larger for higher impaction speeds. It is shown that the strength of the confined shock wave gradually decreases along its propagation. Through the comparison of pressure distributions non-dimensionalized by p_h, it is shown that the weaker the intensity of the shock wave, the more the pressure decays at the same dimensionless instant. Furthermore, for higher impaction speeds, the stronger confined shock wave will reflect off the column surface like to the reflected rarefaction waves. Therefore, the convergence region will be larger for higher impaction speeds.

Consequently, figure 14 shows the pressure contours at the time when the first reflected waves converge for the different impaction speeds. This also corresponds to the time when cavitation occurs, in which the cavitation zone is marked by the isoline of the vapour volume fraction. The impaction speed is equal to, or larger than, 110 m s^{-1}, among the present four chosen speeds, and the convergence of the rarefaction waves can induce the cavitation since the local pressure is below $p_{threshold}$,

https://doi.org/10.1017/jfm.2018.753 Published online by Cambridge University Press

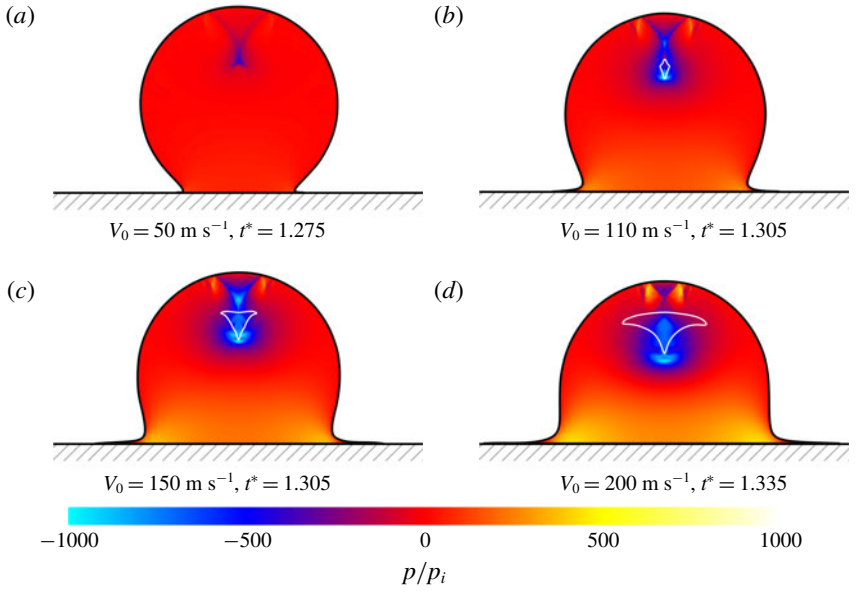


FIGURE 14. (Colour online) Pressure contours when the reflected waves come to focus for different impaction speeds. The time instant is $t^* = 1.275$, 1.305, 1.305 and 1.335, corresponding to the initial impaction speeds of 50, 110, 150 and 200 m s^{-1}, respectively. For (*b–d*) the time also relates to that when the maximum cavitation zone occurs. The white solid line represents the isoline of the vapour volume fraction.

figure 15(*a*), which presents the dimensionless pressure distributions. The cavitation zone becomes larger as the impaction speed increases from 110 to 200 m s^{-1}.

Referring to the distributions of the vapour volume fraction, along the vertical central lines, for the four chosen impaction speeds, figure 15(*b*), the vapour volume fraction rises sharply in the cavitation region and is located between $y/D_0 = 0.45$ and 0.7 for $V_0 = 110$, 150 and 200 m s^{-1}. The profiles of the vapour volume fraction also indicate that the cavitation zone becomes larger for higher impaction speeds ranging from 110 to 200 m s^{-1}.

Figure 16 shows the pressure contours at the moment the cavity (if there is any) collapses completely and shock waves are emitted. In the case of $V_0 = 50$ m s^{-1}, no cavitation is observed, and the reflected rarefaction wave propagates upstream, figure 16(*a*). As shown in figure 16, stronger collapsing waves can be induced by stronger impaction and they need a longer time to collapse. Very complicated structures involving reflected waves, the circular collapsing shock wave and refraction waves evolve inside the column.

In a later stage, a splash will occur for the impacted high-speed droplet, but this is beyond the present research. The contact line dynamics is dominated by the inertial effects of the droplet in the earlier stages of impaction, which occurs irrespective of the physical properties of the liquid and the surface, and the wettability is also not influential (Yarin 2005). Therefore, the analysis of contact line dynamics is also not considered in the present study.

https://doi.org/10.1017/jfm.2018.753 Published online by Cambridge University Press

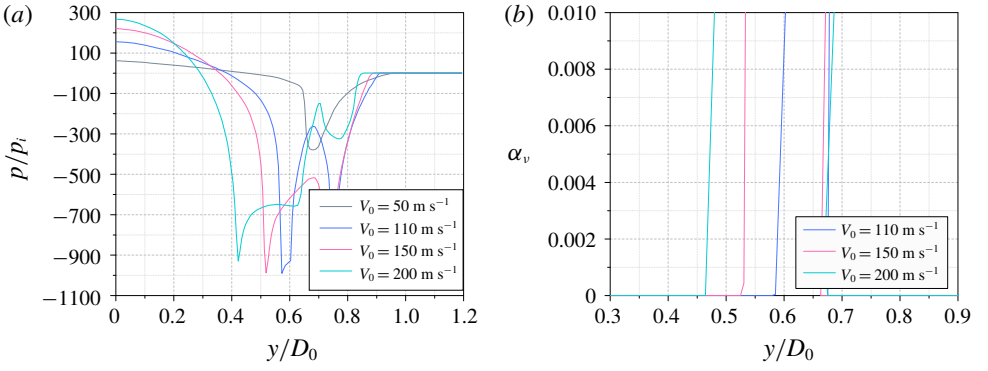


FIGURE 15. (Colour online) Dimensionless pressure (*a*) and vapour volume fraction (*b*) along the vertical central axis for different initial speeds at the times of $t^* = 1.275$, 1.305, 1.305 and 1.335, respectively, which refer to the contours in figure 14.

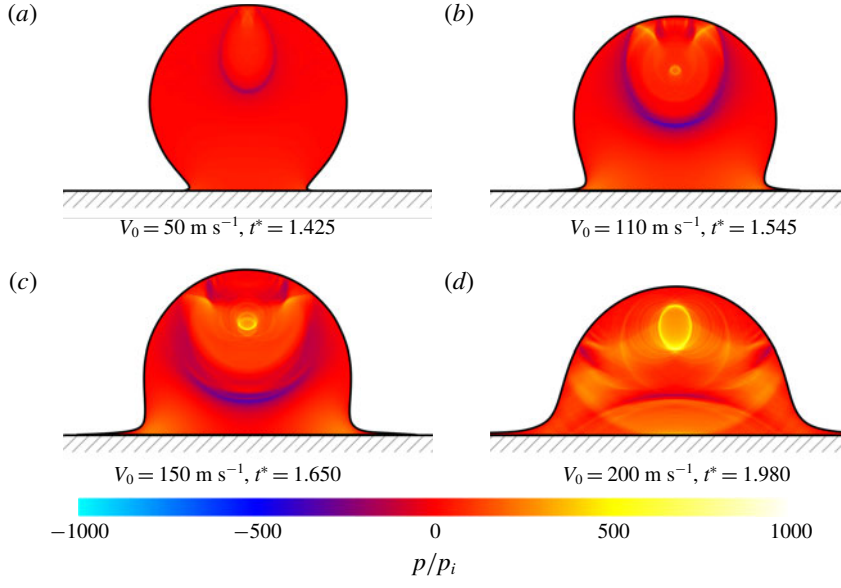


FIGURE 16. (Colour online) Pressure contours at the time the cavities collapse. The time instant is $t^* = 1.425$, 1.545, 1.650 and 1.980, corresponding to the initial impaction speeds of 50, 110, 150 and 200 m s^{-1}, respectively. The shock waves emitted from the collapsing bubble are visible for the cases of $V_0 = 110$, 150 and 200 m s^{-1}.

6. Conclusion and remarks

This study involved a numerical investigation of high-speed cylindrical droplet impingement on a solid wall, and also contributed to the improvement of the phase-transition model and algorithm for the highly compressible two-phase flows. More specifically, the promoted two-phase multi-component compressible fluid model, coupled with a phase-transition model describing the homogeneous cavitation process,

https://doi.org/10.1017/jfm.2018.753 Published online by Cambridge University Press

is used to describe the Eulerian flow system. The phase transition is triggered in the simulation when the local fluid pressure is lower than the threshold value. This is justified by the pressure–temperature expression obtained from the linear approximation of the curve for the cavitation pressure. The numerical chemical potential relaxation process is employed to decouple the solution of the source terms with a hyperbolic operator. Thus, the cavitation evolution process inside the droplet can be captured in detail, which has not been presented in previous work. The analyses of the physical mechanism, such as the generation and propagation of complex wave structures, and the inception and collapsing of the cavity, are then conducted based on the simulation results.

The simulation of the impingement of a 110 m s^{-1} water column on a solid wall reproduced the cavitation inception observed in the experiments and the evolution process of the collapsing of the cavitation zones. A detailed analysis was presented for the above process showing the evolution and interaction of the complicated waves inside the column. The confined shock wave is generated immediately after the impingement of the water column on the wall and it propagates inside the water column. When the contact angle θ is larger than the critical value, the confined shock wave will detach from the solid wall and continually propagate towards the top surface of the column. Meanwhile, the confined shock wave will be reflected by the surface of the liquid column and generate a series of rarefaction waves. The convergence of the rarefaction waves can induce low-pressure regions. Those regions interact and gradually merge at the vertical axis, the position of which is located at approximately one third of the initial diameter away from the top pole. The local fluid state reaches the thermodynamic threshold condition for triggering of the phase transition and cavitation occurs. The capture of the inception of cavitation by the present numerical simulation is consistent with that observed in the experiments. Furthermore, the evolution process of the cavitation zone, including the development and collapse, is further discussed. Once the cavity collapses, a series of shock waves is emitted, which again increase the pressure of the local fluid.

The effects of different initial impaction speeds on droplet dynamics and cavitation structures were investigated. The initial impact speed was chosen as 50, 110, 150 and 200 m s^{-1} respectively. The numerical results showed that the impaction speed has a significant influence on the strength of the confined shock wave, which increases with the impaction speed. For a higher initial speed, the critical contact angle θ_c is larger, and a larger cavitation zone is induced. Larger cavitation zones and stronger collapsing waves are recognized for higher initial impaction speeds. The geometrical morphology of the droplet is abstracted by analysing the two-phase interface structures.

In this study, a conserved Eulerian system was employed. However, even though the viscosity and surface tension can be both neglected in a high-speed impaction process, their effect on the cavitation and collapse should be taken into account, separately or jointly, in the future. Furthermore, the extension studies should be carried out for droplets of different liquids.

Acknowledgements

The authors would like to acknowledge partial financial support from the Natural Science Foundation of China (nos 51676111, 11628206 and NSAF-U1730104), the State Key Laboratory of Chemical Engineering (no. SKL-ChE-16A02) and the Tsinghua University Initiative Scientific Research Program.

https://doi.org/10.1017/jfm.2018.753 Published online by Cambridge University Press

REFERENCES

AHMAD, M., CASEY, M. & SÜRKEN, N. 2009 Experimental assessment of droplet impact erosion resistance of steam turbine blade materials. *Wear* **267** (9), 1605–1618.

ANDO, K., COLONIUS, T. & BRENNEN, C. E. 2011 Numerical simulation of shock propagation in a polydisperse bubbly liquid. *Intl J. Multiphase Flow* **37** (6), 596–608.

AZOUZI, M. E. M., RAMBOZ, C., LENAIN, J. F. & CAUPIN, F. 2013 A coherent picture of water at extreme negative pressure. *Nat. Phys.* **9** (1), 38–41.

BAER, M. R. & NUNZIATO, J. W. 1986 A two-phase mixture theory for the deflagration-to-detonation transition (ddt) in reactive granular materials. *Intl J. Multiphase Flow* **12** (6), 861–889.

BOWDEN, F. P. & FIELD, J. E. 1964 The brittle fracture of solids by liquid impact, by solid impact, and by shock. *Proc. R. Soc. Lond.* A **282** (1390), 331–352.

BRENNEN, C. E. 2013 *Cavitation and Bubble Dynamics*. Cambridge University Press.

CAMUS, J. J. 1971 High speed flow in impact and its effect on solid surfaces. PhD thesis, University of Cambridge.

CAUPIN, F. & HERBERT, E. 2006 Cavitation in water: a review. *C. R. Phys.* **7** (9–10), 1000–1017.

COOK, S. S. 1928 Erosion by water-hammer. *Proc. R. Soc. Lond.* A **119** (783), 481–488.

CORALIC, V. & COLONIUS, T. 2014 Finite-volume WENO scheme for viscous compressible multicomponent flows. *J. Comput. Phys.* **274**, 95–121.

EGGERS, J., FONTELOS, M. A., JOSSERAND, C. & ZALESKI, S. 2010 Drop dynamics after impact on a solid wall: theory and simulations. *Phys. Fluids* **22** (6), 062101.

FIELD, J. E., DEAR, J. P. & OGREN, J. E. 1989 The effects of target compliance on liquid drop impact. *J. Appl. Phys.* **65** (2), 533–540.

FIELD, J. E., CAMUS, J. J., TINGUELY, M., OBRESCHKOW, D. & FARHAT, M. 2012 Cavitation in impacted drops and jets and the effect on erosion damage thresholds. *Wear* **290**, 154–160.

FISHER, J. C. 1948 The fracture of liquids. *J. Appl. Phys.* **19** (11), 1062–1067.

FUSTER, D. & COLONIUS, T. 2011 Modelling bubble clusters in compressible liquids. *J. Fluid Mech.* **688**, 352–389.

GOTTLIEB, S. & SHU, C. W. 1998 Total variation diminishing Runge–Kutta schemes. *Math. Comput. Amer. Math. Soc.* **67** (221), 73–85.

HALLER, K. K., POULIKAKOS, D., VENTIKOS, Y. & MONKEWITZ, P. 2003 Shock wave formation in droplet impact on a rigid surface: lateral liquid motion and multiple wave structure in the contact line region. *J. Fluid Mech.* **490**, 1–14.

HALLER, K. K., VENTIKOS, Y., POULIKAKOS, D. & MONKEWITZ, P. 2002 Computational study of high-speed liquid droplet impact. *J. Appl. Phys.* **92** (5), 2821–2828.

HAN, E., HANTKE, M. & MÜLLER, S. 2017 Efficient and robust relaxation procedures for multi-component mixtures including phase transition. *J. Comput. Phys* **338**, 217–239.

HAN, Y., XIE, Y. & ZHANG, D. 2012 Numerical study on high-speed impact between a water droplet and a deformable solid surface. In *ASME Turbo Expo 2012: Turbine Technical Conference and Exposition*, pp. 675–683. American Society of Mechanical Engineers.

HANSSON, I. & MØRCH, K. A. 1980 The dynamics of cavity clusters in ultrasonic (vibratory) cavitation erosion. *J. Appl. Phys.* **51** (9), 4651–4658.

HERBERT, E. & CAUPIN, F. 2005 The limit of metastability of water under tension: theories and experiments. *J. Phys.: Condens. Matter* **17** (45), S3597.

HEYMANN, F. J. 1969 High-speed impact between a liquid drop and a solid surface. *J. Appl. Phys.* **40** (13), 5113–5122.

JOHNSEN, E. & COLONIUS, T. 2006 Implementation of WENO schemes in compressible multicomponent flow problems. *J. Comput. Phys.* **219** (2), 715–732.

JOSSERAND, C. & THORODDSEN, S. T. 2016 Drop impact on a solid surface. *Annu. Rev. Fluid Mech.* **48**, 365–391.

KONDO, T. & ANDO, K. 2016 One-way-coupling simulation of cavitation accompanied by high-speed droplet impact. *Phys. Fluids* **28** (3), 033303.

LESSER, M. B. 1981 Analytic solutions of liquid-drop impact problems. *Proc. R. Soc. Lond.* A **377** (1770), 289–308.

https://doi.org/10.1017/jfm.2018.753 Published online by Cambridge University Press

MOMBER, A. W. 2006 A transition index for rock failure due to liquid impact. *Wear* **260** (9), 996–1002.

MOMBER, A. W. 2016 The response of geo-materials to high-speed liquid drop impact. *Intl J. Impact Engng* **89**, 83–101.

MÜLLER, I. & MÜLLER, W. H. 2009 *Fundamentals of Thermodynamics and Applications*. Springer.

MUNDO, C. H. R., SOMMERFELD, M. & TROPEA, C. 1995 Droplet-wall collisions: experimental studies of the deformation and breakup process. *Intl J. Multiphase Flow* **21** (2), 151–173.

NIU, Y. Y. & WANG, H. W. 2016 Simulations of the shock waves and cavitation bubbles during a three-dimensional high-speed droplet impingement based on a two-fluid model. *Comput. Fluids* **134**, 196–214.

OBRESCHKOW, D., DORSAZ, N., KOBEL, P., DE BOSSET, A., TINGUELY, M., FIELD, J. & FARHAT, M. 2011 Confined shocks inside isolated liquid volumes: a new path of erosion? *Phys. Fluids* **23** (10), 101702.

OKA, Y. I., MIHARA, S. & MIYATA, H. 2007 Effective parameters for erosion caused by water droplet impingement and applications to surface treatment technology. *Wear* **263** (1), 386–394.

OKA, Y. I. & MIYATA, H. 2009 Erosion behaviour of ceramic bulk and coating materials caused by water droplet impingement. *Wear* **267** (11), 1804–1810.

OKADA, H., UCHIDA, S., NAITOH, M., XIONG, J. & KOSHIZUKA, S. 2011 Evaluation methods for corrosion damage of components in cooling systems of nuclear power plants by coupling analysis of corrosion and flow dynamics (v) flow-accelerated corrosion under single- and two-phase flow conditions. *J. Nucl. Sci. Technol.* **48** (1), 65–75.

PASANDIDEH-FARD, M., QIAO, Y. M., CHANDRA, S. & MOSTAGHIMI, J. 1996 Capillary effects during droplet impact on a solid surface. *Phys. Fluids* **8** (3), 650–659.

PELANTI, M. & SHYUE, K. M. 2014 A mixture-energy-consistent six-equation two-phase numerical model for fluids with interfaces, cavitation and evaporation waves. *J. Comput. Phys.* **259**, 331–357.

PETITPAS, F., FRANQUET, E., SAUREL, R. & LE METAYER, O. 2007 A relaxation-projection method for compressible flows. Part II. Artificial heat exchanges for multiphase shocks. *J. Comput. Phys.* **225** (2), 2214–2248.

REIN, M. 1993 Phenomena of liquid drop impact on solid and liquid surfaces. *Fluid Dyn. Res.* **12** (2), 61–93.

SANADA, T., ANDO, K. & COLONIUS, T. 2011 A computational study of high-speed droplet impact. *Fluid Dyn. Mater. Process.* **7** (4), 329–340.

SANADA, T., WATANABE, M., SHIROTA, M., YAMASE, M. & SAITO, T. 2008 Impact of high-speed steam-droplet spray on solid surface. *Fluid Dyn. Res.* **40** (7), 627–636.

SAUREL, R. & ABGRALL, R. 1999 A multiphase Godunov method for compressible multifluid and multiphase flows. *J. Comput. Phys.* **150** (2), 425–467.

SAUREL, R., BOIVIN, P. & LE MÉTAYER, O. 2016 A general formulation for cavitating, boiling and evaporating flows. *Comput. Fluids* **128**, 53–64.

SAUREL, R. & PETITPAS, F. 2013 Introduction to diffuse interfaces and transformation fronts modelling in compressible media. In *ESAIM: Proceedings*, pp. 124–143. EDP Sciences.

SAUREL, R., PETITPAS, F. & ABGRALL, R. 2008 Modelling phase transition in metastable liquids: application to cavitating and flashing flows. *J. Fluid Mech.* **607**, 313–350.

SEMBIAN, S., LIVERTS, M., TILLMARK, N. & APAZIDIS, N. 2016 Plane shock wave interaction with a cylindrical water column. *Phys. Fluids* **28** (5), 056102.

SOTO, D., DE LARIVIERE, A. B., BOUTILLON, X., CLANET, C. & QUÉRÉ, D. 2014 The force of impacting rain. *Soft Matt.* **10** (27), 4929–4934.

THOMPSON, K. W. 1987 Time dependent boundary conditions for hyperbolic systems. *J. Comput. Phys.* **68** (1), 1–24.

THORODDSEN, S. T., ETOH, T. G., TAKEHARA, K., OOTSUKA, N. & HATSUKI, Y. 2005 The air bubble entrapped under a drop impacting on a solid surface. *J. Fluid Mech.* **545** (-1), 203–212.

https://doi.org/10.1017/jfm.2018.753 Published online by Cambridge University Press

THORODDSEN, S. T., TAKEHARA, K. & ETOH, T. G. 2010 Bubble entrapment through topological change. *Phys. Fluids* **22** (5), 051701.

THORODDSEN, S. T., TAKEHARA, K. & ETOH, T. G. 2012 Micro-splashing by drop impacts. *J. Fluid Mech.* **706**, 560–570.

TITAREV, V. A. & TORO, E. F. 2004 Finite-volume WENO schemes for three-dimensional conservation laws. *J. Comput. Phys.* **201** (1), 238–260.

TORO, E. F. 2013 *Riemann Solvers and Numerical Methods for Fluid Dynamics: A Practical Introduction*. Springer Science & Business Media.

TREVENA, D. H. 1984 Cavitation and the generation of tension in liquids. *J. Phys.* D **17** (11), 2139.

XIANG, G. & WANG, B. 2017 Numerical study of a planar shock interacting with a cylindrical water column embedded with an air cavity. *J. Fluid Mech.* **825**, 825–852.

XIONG, J., KOSHIZUKA, S. & SAKAI, M. 2010 Numerical analysis of droplet impingement using the moving particle semi-implicit method. *J. Nucl. Sci. Technol.* **47** (3), 314–321.

XIONG, J., KOSHIZUKA, S. & SAKAI, M. 2011 Investigation of droplet impingement onto wet walls based on simulation using particle method. *J. Nucl. Sci. Technol.* **48** (1), 145–153.

XIONG, J., KOSHIZUKA, S., SAKAI, M. & OHSHIMA, H. 2012 Investigation on droplet impingement erosion during steam generator tube failure accident. *Nucl. Engng Des.* **249**, 132–139.

YARIN, A. L. 2005 Drop impact dynamics: splashing, spreading, receding, bouncing. *Annu. Rev. Fluid Mech.* **38** (1), 159–192.

ZEIN, A., HANTKE, M. & WARNECKE, G. 2010 Modeling phase transition for compressible two-phase flows applied to metastable liquids. *J. Comput. Phys.* **229** (8), 2964–2998.

ZEIN, A., HANTKE, M. & WARNECKE, G. 2013 On the modeling and simulation of a laser-induced cavitation bubble. *Intl J. Numer. Meth. Fluids* **73** (2), 172–203.

https://doi.org/10.1017/jfm.2018.753 Published online by Cambridge University Press